A quantitative study of particle size effects in the magnetorelaxometry of magnetic nanoparticles using atomic magnetometry

V. Dolgovskiy [a], V. Lebedev [a,*], S. Colombo [a], A. Weis [a], B. Michen [c,1], L. Ackermann-Hirschi [c], A. Petri-Fink [c,b]

[a] Physics Department, University of Fribourg, CH-1700 Fribourg, Switzerland
[b] Chemistry Department, University of Fribourg, CH-1700 Fribourg, Switzerland
[c] Adolphe Merkle Institute, University of Fribourg, CH-1700 Fribourg, Switzerland

The discrimination of immobilised superparamagnetic iron oxide nanoparticles (SPIONs) against SPIONs in fluid environments via their magnetic relaxation behaviour is a powerful tool for bio-medical imaging. Here we demonstrate that a gradiometer of laser-pumped atomic magnetometers can be used to record accurate time series of the relaxing magnetic field produced by pre-polarised SPIONs. We have investigated dry *in vitro* maghemite nanoparticle samples with different size distributions (average radii ranging from 14 to 21 nm) and analysed their relaxation using the Néel–Brown formalism. Fitting our model function to the magnetorelaxation (MRX) data allows us to extract the anisotropy constant K and the saturation magnetisation M_S of each sample. While the latter was found not to depend on the particle size, we observe that K is inversely proportional to the (time- and size-) averaged volume of the magnetised particle fraction. We have identified the range of SPION sizes that are best suited for MRX detection considering our specific experimental conditions and sample preparation technique.

1. Introduction

Due to their unique magnetic properties, superparamagnetic iron oxide nanoparticles (SPIONs) are very promising materials for diagnostic and therapeutic biomedical applications [1–3]. SPIONs are used, e.g., as contrast agents in magnetic resonance imaging (MRI), where they enhance the local magnetic field, thereby improving the proton magnetic resonance signals [4]. The biocompatibility of surface-functionalised SPIONs gives them a high potential for therapeutic applications, such as hyperthermia treatment [5] or drug delivery [6].

The SPIONs' superparamagnetism is due to their single domain structure and the ensuing properties of low saturation magnetisation M_s and nonlinear $M(H)$ response in low (mT) fields are key properties for imaging SPION distributions in biological tissues. Imaging may serve the purpose of representing specific biological entities (organ, tumor, cell, etc.) when tagging those entities by specifically coated SPIONS. On the other hand, SPION imaging is a prerequisite for monitoring the efficiency of drug delivery in therapeutic applications.

Magnetic particle imaging, MPI [7], is a rapidly developing imaging method that builds on the generation of harmonic signals $M(t)$ when SPIONs are excited by a monochromatic field $H(t)$ oscillating around $H = 0$. Recently, MPI devices have become commercially available [8].

The present paper deals with magnetorelaxation, MRX, an alternative SPION detection method [9] that is widely spread, and whose extension to imaging SPION volume distributions is slowly emerging. MRX consists in magnetising the SPIONS by a moderate (mT) static external magnetic field H_M during a time T_M and detecting the sample's decaying magnetisation $M(t)$ following that magnetisation. $M(t)$ is monitored by one or several sensitive magnetometers that record the induction $B_{MRX}(t) \propto M(t)$. Quantities of interest are the initial amplitude $B_{MRX}(0)$ and the specific time dependence of the decay process. For strictly monodisperse particles with identical radii r one expects an exponential decay law with an r-dependent time constant. In practice one deals with samples that have specific size distributions $f_{NP}(r)$ which implies a non-trivial non-exponential decay, since both the magnetisation process and the decay process are particle size dependent.

The magnetisation of immobilised SPIONs, i.e., nanoparticles embedded in a solid matrix or bound to the surface of a biological entity relaxes by an internal reorientation of the magnetisation inside of the particle. The time dependence of this Néel relaxation

process [10] is characterised by a time constant

$$\tau_N = t_0 e^{KV/k_B T}, \tag{1}$$

where K is the anisotropy constant and V the particle core volume. Conversely, SPIONs dispersed in a liquid of viscosity η, relax by rotational diffusion of the particles (and hence their magnetic moments) with a time constant given by [11]

$$\tau_B = \frac{\eta V_{\mathrm{hydro}}}{k_B T}, \tag{2}$$

where V_{hydro} is the hydrodynamic volume of the nanoparticle. One speaks of the Brownian relaxation in the latter case. Because of the exponential particle size dependence, the Néel relaxation is orders of magnitude slower than the Brownian relaxation for sufficiently large particles (for reasonable material parameter values $\tau_B \approx \tau_N$ for particles with radii of 10–11 nm). This feature allows the discrimination of particles bound to specific biological entities [12] from particles embedded in body fluids, thus forming the basis for SPION imaging by MRX. The property was used, e.g., to image the accumulation of intravenously injected SPIONs in the spleen and liver of a mouse by MRX [13], or to quantify the aggregation of magnetic nanoparticles in cell cultures [14]. Many of the earlier studies used multi-core particles, while more recently larger single-core magnetic particles have shown large magnetic signals in observation windows ranging from 50 ms to 2 s [15]. Those and others studies [16–18] have demonstrated that (SQUID-based) MRX has a high potential for biomedical imaging applications.

In view of detecting SPIONs at the lowest possible concentrations, MRX calls for sensors with a high magnetometric sensitivity. In the past, SQUIDs (superconducting quantum interference devices) have been the detectors of choice for detecting the weak magnetic fields produced by the MRX process. Recent developments in the field of atomic magnetometry provide a promising alternative to SQUIDs for detecting weak magnetic fields [19]. Atomic magnetometers do not require cryogenic cooling and offer the potential for miniaturisation and easily configurable sensor array structures. Atomic magnetometer arrays have been used to map the dynamics of the magnetic field generated by the human heart (magnetocardiography) [20] or by the human brain activity [21]. More recently they have been used for MRX detection [22,23], and were shown to yield similar results than SQUID-based MRX [22]. Atomic magnetometers have also demonstrated a high sensitivity for detecting cancer cells tagged by antibody-coated SPIONs [24].

MRX detection faces the following problem: small-sized SPIONs are more easily magnetised than large-sized particles. At the same time the magnetisation of the smaller particles decays more rapidly than the larger SPIONs' magnetisation. The magnetisation typically occurs in ~mT fields, while the MRX signals are recorded down to the pT (or even fT) level. To our knowledge there is no magnetometer whose dynamic range covers the corresponding ≈ 10 orders of magnitude in detectable fields. In general the magnetometers are strongly perturbed during the magnetisation pulse and need a recovery (dead) time τ_D, between switching off the magnetising field and recording the time dependent field of interest. This dead time is determined, e.g., by the recovery of electronic feedback loops or the slow decay of eddy currents in nearby conductors. MRX systems equipped with a SQUID or fluxgate sensor have typically $\tau_D > 100$ µs, while a novel CMOS Hall-effect magnetometer has recorded relaxation after $\tau_D = 100$ ns [25], although at the cost of a strongly reduced magnetometric sensitivity. Long dead times therefore prevent the detection of small particles because of their shorter relaxation times. In order to determine the optimal SPION size distributions for specific MRX measurements one has to consider the complex interplay between the material constants (M_s and K) and the

experimental parameters (H_M, T_M, and τ_D) that determines the MRX signal, i.e., $B_{\mathrm{MRX}}(t)$.

For the studies described below, we have used a first order gradiometer formed by two laser-driven optically pumped cesium magnetometers and show that these magnetometers yield reliable, high accuracy MRX data. We have performed a systematic study of oleic acid coated SPION samples of different size distributions and concentrations produced by thermal decomposition of oleate complexes. In-house produced samples are compared to commercial samples.

A model function describing the $B(t)$ dependence is derived and its fit to the experimental MRX data allows us to infer the anisotropy constant K and the saturation magnetisation M_s for all samples. In the range of investigated particle size distributions we find a $1/V_{\mathrm{act}}$ dependence on the (time- and size-averaged) volume V_{act} of the magnetically active particles. We have further analysed the dependence of the absolute value of the recorded magnetic field on the iron content of the different samples.

The paper is organised as follows. In Section 2 we describe the methods used to produce and characterise the samples, and describe the working principle of the deployed magnetometer. In Section 3 we derive the magnetisation build-up and relaxation model used for interpreting the experimentally recorded magnetic induction signals, while Section 4 describes the data treatment and fitting procedures. In Section 5 we collect the results of the measurements and their analysis and in Section 6 we summarise the performed investigations.

2. Material and methods

2.1. SPIONs

The nanoparticles were synthesised following the method by Park et al. [26]. The method relies on the thermal decomposition of iron oleate complexes and results in oleate stabilised SPIONs. Adjusting the reaction conditions, i.e., boiling point of the solvent or oleic acid concentration, allows tailoring the particle size [27]. Briefly, sodium oleate and ferric chloride hexahydrate (Sigma-Aldrich) were used to prepare the iron–oleate complex. In a next step, the oleate was mixed with oleic acid at a molar oleate/oleic ratio of 2.2 in trioctylamine or docosane. The mixture was then heated to 320 °C (trioctylamine) or 340 °C (docosane) under vigorous stirring for 1 h at constant temperature, after which the nanoparticles were separated by centrifugation, washed with ethanol and dispersed in hexane. In addition to three sets of in-house produced SPIONs (samples A, B, and C), three other sets of SPIONs (SOR-25, SOR-30, and SOR-40) (referred to hereafter as D, E, and F, respectively), with different size distributions were purchased from Ocean Nanotech (AR, USA). The Ocean Nanotech particles were also synthesised by a thermal decomposition route, comparable to our in-house produced batches. The iron content of all samples was determined by redox-titration with potassium permanganate. SPION suspensions were filled into non-magnetic flat 8 mm diameter cylindrical dishes and dried overnight at 60 °C in an oven.

2.2. Characterisation of particle size distribution

A 75 kV transmission electron microscope (Hitachi, H-7100, Tokyo, Japan) was used to determine the nanoparticle size distributions. Electron micrographs were recorded with a Morada CCD digital camera (Olympus, Tokyo, Japan) and saved as 16-bit TIFF images. These raw files were binarised using an IsoData-based threshold method and analysed using the Fit Ellipse algorithm in ImageJ. Because all samples showed a fairly spherical geometry
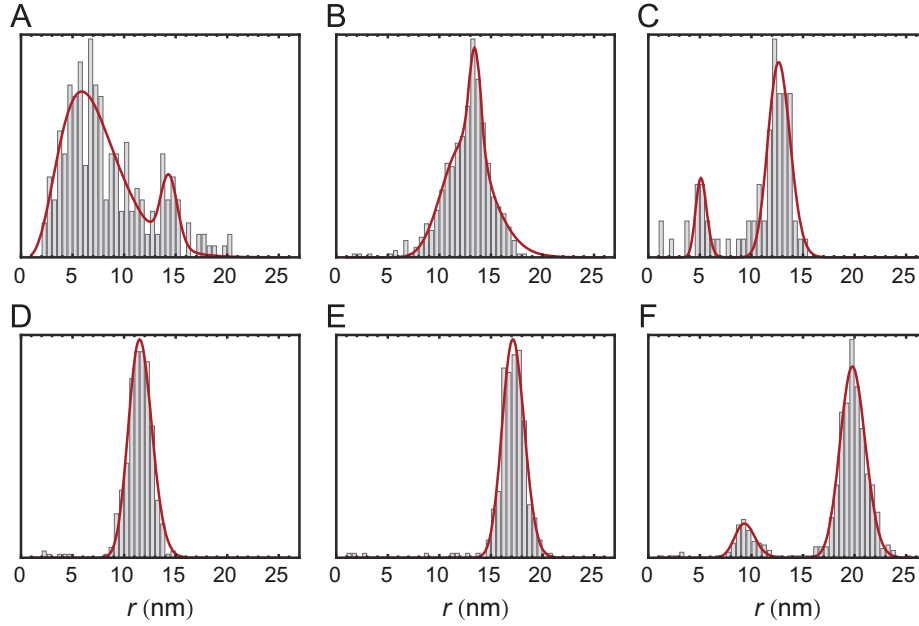
Fig. 1. Particles size distributions of samples A–F, together with (solid lines) fitted Schulz–Zimm functions $f_{SZ}(r)$ (Eq. (3)).

(aspect ratios <1.15), effective radii were assigned to the particles by assuming circular shapes of equal area as the measured ellipses. At least five images of each sample were analysed resulting in a total of more than 100 particle counts for each sample. The size distributions are presented as histograms with a bin size of 0.5 nm and fitted assuming one- or two-component Schulz–Zimm distribution functions (Fig. 1)

$$f_{SZ}(r) = \frac{1}{\Gamma(k)}\left(\frac{k}{r_{avg}}\right)^k r^{k-1} \exp\left(-k\frac{r}{r_{avg}}\right),$$

(3)

where $r_{avg} = \int_0^\infty r f_{SZ}(r)\,\mathrm{d}r$ is the average particle radius. The parameter k is related to the *rms* width of the distribution by $\Delta r_{rms} = r_{avg}/\sqrt{k}$.

2.3. MRX measurements by atomic magnetometers

We have performed systematic series of magnetorelaxation (MRX) measurements on all six SPION samples at different concentrations. The magnetic field produced by each SPION sample following its magnetisation by a static field and the decay of that magnetisation (MRX signal) was recorded by a first order gradiometer formed by two laser-pumped Cs magnetometers (CsOPM) as shown in Fig. 2. This single channel gradiometer is a subset of the array of 19 (second-order) gradiometers that we have used in the past to monitor the dynamics of human magnetocardiography maps [20].

The magnetometer set-up is mounted in a double-walled aluminium chamber in which the geomagnetic field is compensated and a vertical homogeneous offset field B_0 of 10 μT is applied to the magnetometers.
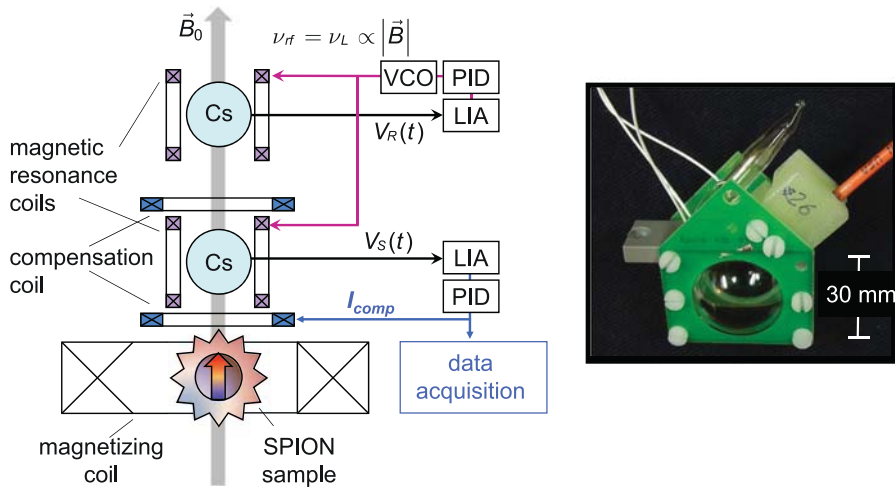
Fig. 2. Left: Principle of the first-order CsOPM gradiometer. The upper (reference) magnetometer is forced to oscillate at a frequency that is proportional to the ambient magnetic field and thus tracks field changes in a phase-coherent manner. The lower (sensing) magnetometer measures the gradient that originates from the vertical component of the SPIONs' magnetic field. LIA: lock-in amplifier; PID: proportional-integral-differential amplifier; VCO: voltage-controlled oscillator. Right: Single CsOPM sensor with 30 mm diameter Cs vapour cell and printed circuit boards carrying the magnetic resonance driving rf coils. Laser light is brought to the sensor by a multimode fibre (from top-right) and the miniature (from top-left) coax cables drive the rf coils and send the photocurrent to the control electronics.

3

Each magnetometer uses optically detected magnetic resonance in room temperature Cs vapour that is contained in a paraffin-coated [28] 30 mm diameter Pyrex bulb. In its M_x-mode of operation [29] each sensor produces an oscillatory voltage, $V_i(t)$, that represents the photocurrent from a photodiode detecting the laser power transmitted by the cell. The oscillation frequency is given by the magnetic resonance drive frequency ν_{rf}. On resonance, i.e., when the Cs atoms' Larmor frequency

$$\nu_L \propto |\vec{B}_{tot}| \approx |\vec{B}_0 + (\delta\vec{B}_{MRX} \cdot \hat{B}_0)\hat{B}_0| \tag{4}$$

matches ν_{rf}, the oscillation amplitude is maximal and the oscillation is dephased by $-90°$ with respect to the rf drive. $\delta\vec{B}_{MRX}$ represents the magnetic field of interest and (4) shows that for $|\delta\vec{B}_{MRX}| \lesssim_i |\vec{B}_0|$, the frequency change and hence the phase change is proportional to the component of $\delta\vec{B}_{MRX}$ along the offset field $\vec{B}_0$.

The phase of $V_i(t)$ with respect to the rf drive field is extracted by a digital lock-in amplifier (LIA) [20] and drives, after suitable amplification, a voltage-controlled oscillator (VCO) producing the oscillatory current for the magnetic resonance coils (Fig. 2).

In the upper sensor (reference magnetometer) this phase-locked feedback loop thus locks the magnetometer's oscillation frequency to the magnetic field, thereby correcting any drifts of the ambient and offset fields during data recording. The same oscillation frequency is used to drive the magnetic resonance in the lower sensor (sensing magnetometer) such that any field gradient, i.e., difference of the magnetic fields at the two sensor locations, results in a phase shift of the sensing magnetometer's oscillation. The latter phase shift is then used in a second feedback loop that controls the local field at the sensing magnetometer's location (using compensation coils) in such a way as to stabilise that field to the same value as the field seen by the reference magnetometer. In this way the correction current through the compensation coil is directly proportional to difference of the fields at the two sensor locations, which is easily calibrated based on the correction coils' geometry.

The dishes with the SPION samples were mounted at a distance of 42(2) mm below the centre of the sensing magnetometer cell. The samples were magnetised for $T_M = 3$ s in a vertically oriented magnetic field of $\mu_0 H_M = 27$ mT. The actual MRX recording was initiated ≈ 1 ms after switching off the magnetising field.

3. Superparamagnetic relaxation model

In this section we will develop a quantitative model which relates the experimentally recorded MRX signal $B_{MRX}(t)$ to the sample properties and specific experimental parameters. The model follows closely the one presented in the seminal work by Chantrell et al. [30]. In the latter publication it was shown that $B_{MRX}(t) \propto \ln(1 + \tau_C/t)$ under some simplifying assumptions. Our high accuracy experimental $B_{MRX}(t)$ recordings showed deviations from that simple logarithmic decay law for most of the investigated samples. For this reason we have dropped the simplifying assumption and have applied the more complete underlying model given in [30], also known as moment superposition model (MSM) [31]. We will compare the MSM predictions with those of the simplified model for specific particle size distributions.

3.1. Energy of a SPION in a magnetic field

A (single domain) superparamagnetic particle of volume V has a permanent magnetic moment $\vec{\mu}_p$ that can be expressed in terms of the particle's saturation magnetisation M_s

$$\vec{\mu}_p = \mu_p \hat{\mu} = M_s V \hat{\mu}, \tag{5}$$

where $\hat{\mu}$ is the moment's orientation. Because of their crystalline structure, such particles have a magnetic anisotropy, characterised by preferential directions, called easy axes. Those axes are a natural choice to describe the particle's orientation in space. The magnetic moment minimises its internal potential energy (anisotropy energy E_a) when it is oriented along one of those axes.

Maghemite has a cubic crystal lattice with three orthogonal easy axes and the anisotropy energy, to lowest order, is given by [32]

$$E_a = KV\left(e_x^2 e_y^2 + e_x^2 e_z^2 + e_y^2 e_z^2\right), \tag{6}$$

where (e_x, e_y, e_z) is the magnetic moments' orientation in the coordinate frame spanned by the easy axes. In the laboratory frame the magnetic moment's orientation is described by $\hat{e}'$, related to the orientation in the particle frame by

$$\hat{e}' = R(\varphi, \vartheta, \psi)\hat{e}, \tag{7}$$

where R, with Euler angles φ, ϑ and ψ, is the rotation operator that transforms the easy axes frame to the laboratory frame.

When the particle is exposed to an external magnetic field $\vec{H}$ (chosen to define the laboratory z-axis), it acquires a magnetic interaction energy:

$$E_H(\theta) = -\mu_0 \vec{\mu}_p' \cdot \vec{H} = -\mu_0 \mu_p H \cos\theta \tag{8}$$

that adds to the anisotropy energy, yielding

$$E_{tot}(\varphi, \vartheta, \psi; \theta) = KV\left(e_x'^2 e_y'^2 + e_x'^2 e_z'^2 + e_y'^2 e_z'^2 - 2h\cos\theta\right) \tag{9}$$

where

$$h = \frac{H}{H_K} \quad \text{with} \quad H_K = \frac{2K}{\mu_0 M_s}, \tag{10}$$

H_K being the so-called anisotropy field.

Appendix A illustrates the relative importance of the anisotropy energy and the magnetic energy in the simple case of a uniaxial crystal.

3.2. SPIONs with random orientation: the Langevin function

For a sample with randomly distributed orientations the average total energy $\overline{E}_{tot}$ is given by

$$\overline{E}_{tot}(\theta) = \frac{1}{8\pi^2} \int_0^{2\pi} d\varphi \int_{-1}^1 d(\cos\vartheta) \int_0^{2\pi} d\psi \, E_{tot}(\varphi, \vartheta, \psi; \theta) \tag{11}$$

which yields, using (9),

$$\overline{E}_{tot}(\theta) = \frac{KV}{5} - \mu_0 H M_s V \cos\theta. \tag{12}$$

In thermal equilibrium at temperature T, $\overline{E}_{tot}(\theta)$ obeys a Boltzmann distribution. Because of the axial symmetry imposed by the magnetic field, only the magnetic moment component along the field will have a non-vanishing equilibrium value:

$$\mu_z^{eq} \equiv \langle \vec{\mu}_p \cdot \hat{H} \rangle = \frac{\int_0^\pi \exp\left(-\frac{\overline{E}_{tot}(\theta)}{k_B T}\right) M_s V \cos\theta \sin\theta \, d\theta}{\int_0^\pi \exp\left(-\frac{\overline{E}_{tot}(\theta)}{k_B T}\right) \sin\theta \, d\theta} \equiv M_s V L(x), \tag{13}$$

where

$$L(x) = \coth x - \frac{1}{x} \quad \text{with} \quad x = \frac{\mu_0 H M_s V}{k_B T}, \tag{14}$$

is the Langevin function. In view of the particle size dependencies addressed below we consider $L(x)$ to be a function of particle

4

radius, viz., $L(r)$. We note that the argument of the Langevin function does not depend on the anisotropy constant K, but does depend on the saturation magnetisation M_s.

3.3. Time evolution of the sample magnetisation

When an unpolarised ensemble of particles is exposed to an external magnetic field $H = H_M \equiv hH_K$ during a time T_M it acquires an equilibrium magnetic moment given by [11]

$$\mu_M(H_M, T_M) = \mu_z^{eq}(H_M)\left[1 - \exp(-T_M/\tau_H)\right]. \tag{15}$$

When H_M is switched off at time $t = 0$, the magnetic moment decays according to

$$\mu_z(t) = \mu_M(H_M, T_M)\exp(-t/\tau_0), \tag{16}$$

where $\tau_0 = \tau_{H_M=0}$. Note that the relaxation time constants in both cases differ, because of the H-dependent energy landscape illustrated in Fig. A13. We stress that the time constants also depend on the particle size, an essential feature of the effects studied in this work. Realistic nanoparticle samples are characterised by a distribution function $f_{NP}(r)$ according to

$$dN(r) = N_{tot}f_{NP}(r)\,dr \tag{17}$$

where the total number of SPIONs in the sample, N_{tot}, can be expressed by the total sample mass, m_{tot}, and the average mass, $\langle m \rangle$, of a single particle as

$$N_{tot} = \frac{m_{tot}}{\langle m \rangle} = \frac{m_{tot}}{\rho\langle V \rangle}. \tag{18}$$

In the latter expression ρ is the maghemite density and the average particle volume is given by $\langle V \rangle = \int_0^\infty V(r)f_{NP}(r)\,dr$.

We assume that particles of radius r have been magnetised during a time T_M in a field H_M that is switched off at time $t = 0$. From Eqs. (13), (15) and (16) it follows that the (orientationally averaged) magnetic moment per particle at time t is then given by

$$\mu_z(r, t) = M_sVL(r)\left[1 - e^{-T_M/\tau_H}\right]e^{-t/\tau_0}. \tag{19}$$

The total magnetic moment of particles with radii in the interval $[r, r + dr]$ is

$$d\mu_z(t) = \mu_z(r, t)\,dN(r) \tag{20}$$

$$d\mu_z(t) = \frac{m_{tot}}{\rho\langle V \rangle}f_{NP}(r)M_sV(r)L(r)[1 - e^{-T_M/\tau_H}]e^{-t/\tau_0}\,dr, \tag{21}$$

so that the total magnetic moment of the sample at time t becomes

$$\mu_z(t) = \frac{m_{tot}M_s}{\rho\langle V \rangle}\int_0^\infty V(r)L(r)f_{NP}(r)\Lambda(r, t)\,dr, \tag{22}$$

where

$$\Lambda(r, t) = e^{-t/\tau_0}\left[1 - e^{-T_M/\tau_H}\right] \tag{23}$$

is a function of central importance that we refer to as *window function*.

The on-axis magnetic field detected in the MRX experiments by a magnetometer located at distance R ($\hat{R} = \hat{H}_M$) in the far field of the sample is

$$B(t) = \frac{\mu_0}{2\pi}\frac{\mu_z(t)}{R^3}. \tag{24}$$

Inserting Eqs. (22) and (23) into (24) one obtains the final expression for the magnetic field:

$$B_{MRX}(t) = \frac{\mu_0}{2\pi R^3}\frac{m_{tot}}{\rho}\frac{M_s}{\langle r^3 \rangle}\int_0^\infty L(r)\Lambda(r, t)f_{NP}(r)r^3\,dr, \tag{25}$$

which represents the MRX signal at the sensor position.

3.4. Structure of the window function

The window function (23) can be written as

$$\Lambda(r, t) = e^{-t/\tau_0}\left[1 - e^{-T_M/\tau_H}\right] \equiv e^{-\xi_0(r,t)}\left[1 - e^{-\xi_H(r)}\right]. \tag{26}$$

For a uniaxial particle in a weak ($h \lesssim 1$) magnetic field oriented along the easy axis the time constant τ_H in (26) is given by [11]

$$\frac{1}{\tau_H} = \frac{1}{t_0}(1 - h^2)\left[(1 - h)e^{-\sigma(r)(1-h)^2} + (1 + h)e^{-\sigma(r)(1+h)^2}\right], \tag{27}$$

where σ depends on the anisotropy energy

$$\sigma = \frac{E_a}{k_BT} = \frac{KV}{k_BT}. \tag{28}$$

The constant τ_0 in (26) becomes

$$\frac{1}{\tau_0} = \frac{2}{t_0}e^{-\sigma(r)}, \tag{29}$$

an expression that coincides with the result of Néel [10]. The forefactor is given by

$$\frac{1}{t_0} \approx \gamma^2\eta\left(\frac{4VK^3}{\pi k_BT}\right)^{1/2}, \tag{30}$$

an expression valid for low-dissipation crystals, in which $\eta \lesssim (\gamma M_s)^{-1}$, where γ is the particle's gyromagnetic ratio and η a dissipation constant. With typical values for the particle volume V, and K values from literature, one finds $t_0 \approx 10^{-9}$ s. Generalisations (see, e.g., [33]) of Brown's expression (27) to other crystalline structures lead to similar expressions in which t_0 and $e^{-\sigma}$ also appear as key constituents.

As illustrated in Fig. 3, the particle size dependencies of the two factors in (26) are represented by two sigmoid functions, each varying in the interval [0, 1], their product thus yielding a pulse-shaped window that defines the range of particles contributing to the MRX signal.

For particle size distributions $f_{SZ}(r)$ that are much broader than the widths of the window boundaries, one may replace those boundaries by sharp step functions. This was actually done in the approach described by Chantrell et al. [30], who derived
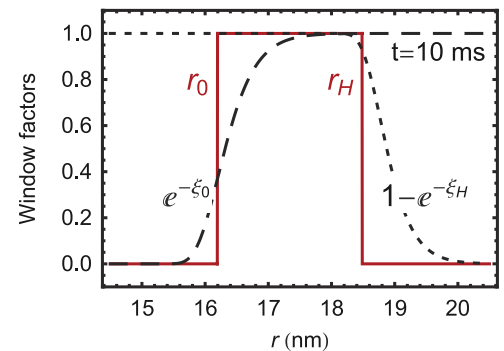
Fig. 3. Dashed and dotted lines represent the r-dependence of the two factors defining the window function $\Lambda(r, t)$ given by Eq. (26). All functions were calculated for $T_M = 3$ s, $\mu_0H_M = 27$ mT, $K = 3.75$ kJ/m³, and $M_s = 19.2$ kA/m. The solid lines represent the sharp-edged window introduced by Chantrell et al. [30].

5
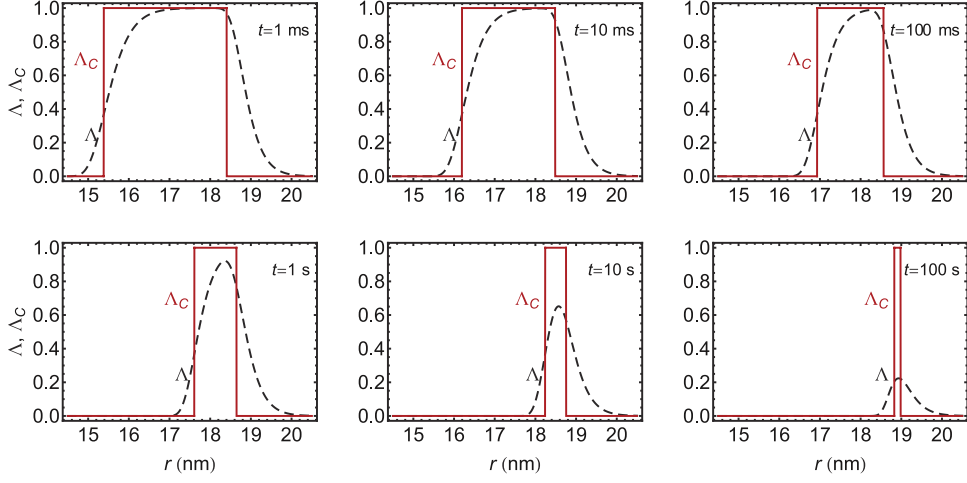
Fig. 4. Time evolution of the window function $\Lambda(r, t)$ given by Eq. (26) evaluated for $T_M = 3$ s, $\mu_0 H_M = 27$ mT, $K = 3.75$ kJ/m^3, and $M_s = 19.2$ kA/m (dashed lines). The solid lines represent the corresponding sharp-edged window $\Lambda_C(r, t)$ used by Chantrell et al. [30].
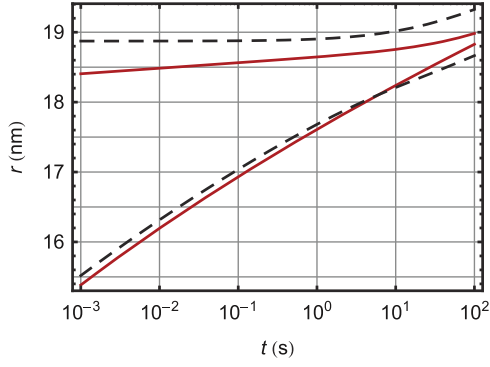
Fig. 5. Time evolution of the left and right boundaries of the window function $\Lambda(r, t)$ for the MSM (dashed lines) and the Chantrell (solid line) models, respectively. The dependencies were calculated with the same set of parameters as in Fig. 4. For the Chantrell model the window boundaries are defined by r_0 (Eq. (32)) and r_H (Eq. (31)), while for the MSM the half-height radii were taken.

$$r_0 = \left[\frac{3}{4\pi} \frac{k_B T}{K} \ln \frac{t}{t_0} \right]^{1/3}$$

(31)

for the lower window boundary, and

$$r_H = \left[\frac{3}{4\pi} \frac{k_B T}{K} \ln \frac{T_M e^{2\sigma_0 h - \sigma_0 h^2} + t}{t_0} \right]^{1/3},$$

(32)

for the upper boundary, where $\sigma_0 = KV_0/k_B T = \ln(t/t_0)$ is the anisotropy energy ratio of particles with a volume V_0 corresponding to the lower boundary radius. The value of the upper boundary r_H increases with growing H_M and T_M, which reflects the fact that the application of a strong field for a long time magnetises particles of ever larger size.

3.5. Window function dynamics and MRX decay

The upper window boundary, determined by $\xi_H(r)$, does not depend on time, while the lower boundary, determined by $\xi_0(r, t)$, moves towards larger radii as time progresses, thereby narrowing the range of particles contributing to the MRX signal. The upper
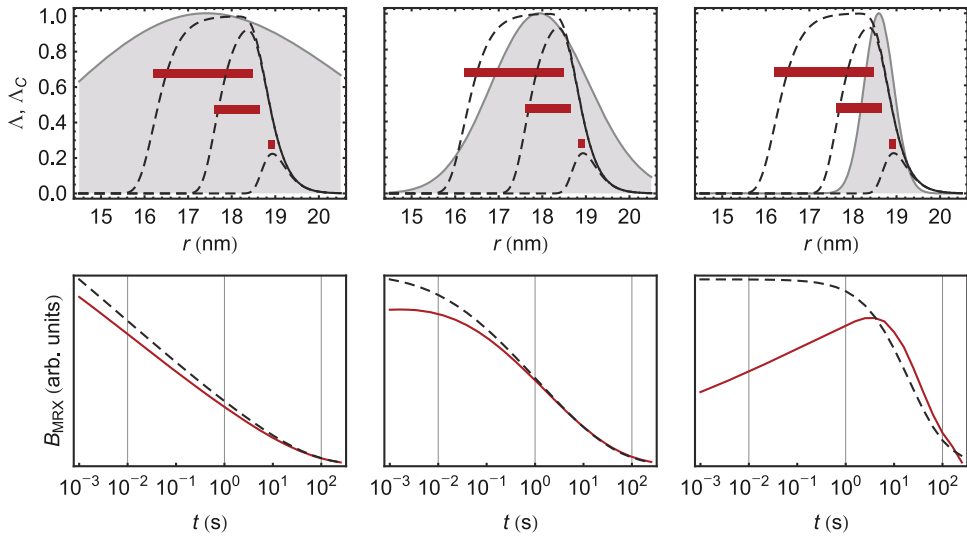
Fig. 6. Predicted MRX signals from nanoparticles with different hypothetical size distributions (left to right). Top: Size distributions (shaded surfaces) and window functions of complete model (dashed lines) and in Chantrell approximation (solid bars) shown for $t = 10$ ms, 1 s and 100 s ($T_M = 3$ s, $\mu_0 H_M = 27$ mT, $K = 3.75$ kJ/m^3, $M_s = 19.2$ kA/m). Bottom: Corresponding decay curves predicted by complete model (dashed lines) and Chantrell approximation (solid line).
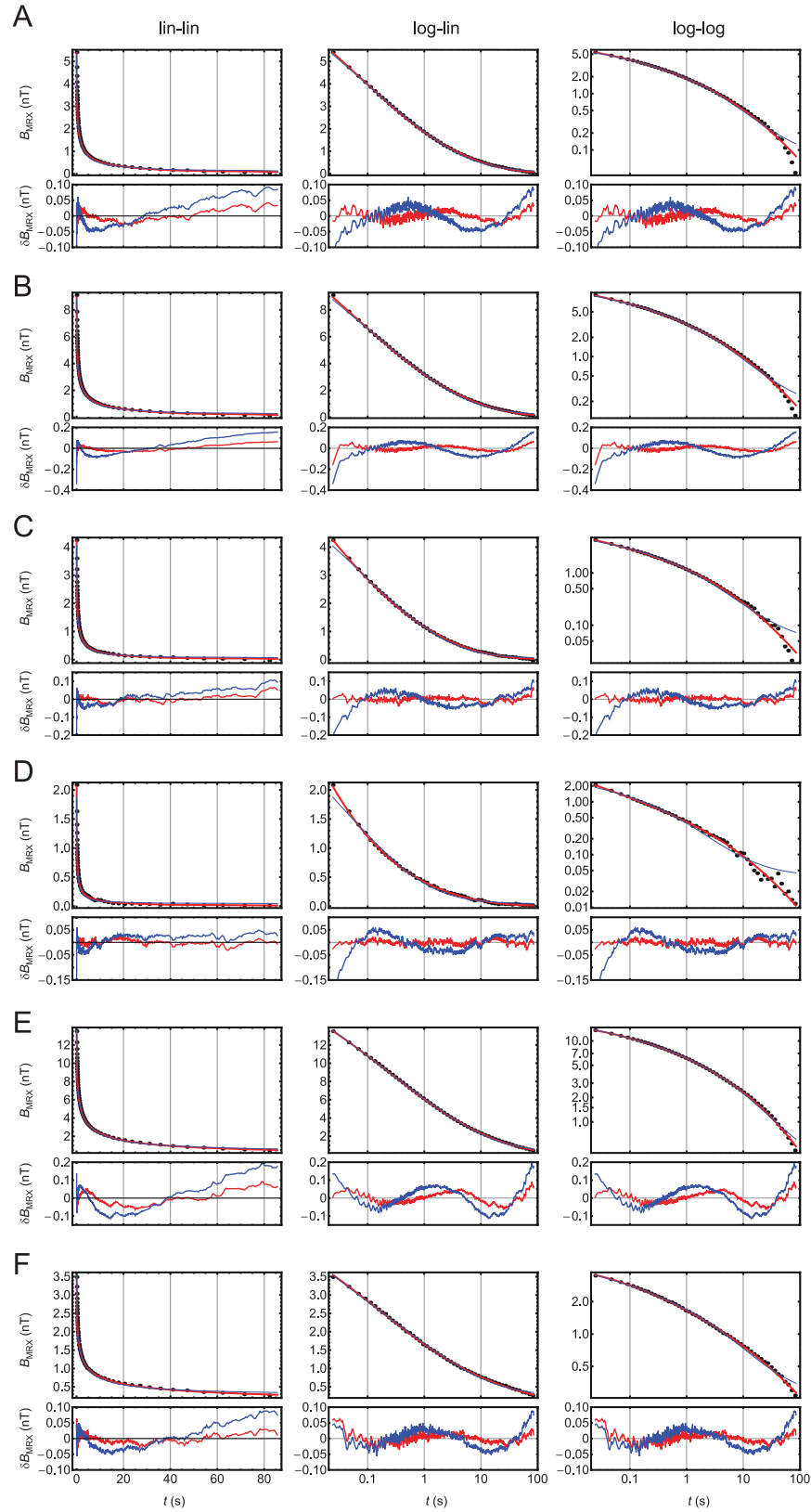
Fig. 7. MRX signals $B_{\mathrm{MRX}}(t)$ of all investigated SPION samples in their highest concentrations, together with fit residuals $\delta B_{\mathrm{MRX}}(t)$. Black dots: experimental data, black and red lines represent fits by the MSM model (34) and Chantrell model (33), respectively. The three columns represent the same data in different combinations of linear and logarithmic scales. (For interpretation of the references to colour in this figure caption, the reader is referred to the web version of this paper.)

boundary is fully determined by the magnetisation process, and the moving lower boundary reflects the faster relaxation of smaller particles. In Fig. 4 we show the time evolution of $\Lambda(r, t)$ for

a reasonable set of the relevant experimental parameters H_M, T_M, M_s, and K. Note that time progresses in logarithmic steps in the figure.

Table 1

Major size-related parameters of the samples A–F and material parameters K and M_s obtained from fits of the MSM function (37) to the MRX curves. The anisotropy energy is calculated according to $E_a = K\langle V\rangle_{\text{act}}$.

Sample	$\langle r\rangle$ (nm)	$\langle r^3\rangle^{1/3}$ (nm)	$\langle r\rangle_{\text{act}}$ (nm)	$\langle r^3\rangle_{\text{act}}^{1/3}$ (nm)	$\langle V\rangle$ (10^3 nm^3)	$\langle V\rangle_{\text{act}}$ (10^3 nm^3)	K (kJ/m^3)	M_s (kA/m)	E_a (10^{-20} J)
A	8.0	9.5	15.2	15.2	3.58	14.85	6.03(10)	21(5)	8.96(15)
B	13.0	13.4	14.4	14.4	10.03	12.44	7.24(19)	21(2)	9.0(2)
C	11.5	12.1	14.3	14.3	7.45	12.30	7.1(3)	19(6)	8.8(3)
D	11.6	11.7	14.4	14.4	6.75	12.51	6.9(3)	24(14)	8.7(4)
E	17.2	17.3	18.0	18.1	21.6	24.6	3.75(5)	19(3)	9.24(12)
F	18.6	19.2	21.1	21.1	29.5	39.5	2.40(5)	20(65)	9.47(19)

Table 2

Fit parameter of the Chantrell function (38) for the MRX curves.

Sample	$\langle r\rangle_{\text{act}}$ (nm)	a_C (nT)	τ_c (s)
A	15.2	0.97(5)	5.4(1.3)
B	14.4	1.55(10)	6.3(1.7)
C	14.3	0.84(8)	2.7(9)
D	14.4	0.48(11)	1.1(6)
E	18.0	2.1(9)	16(4)
F	21.1	0.51(3)	16(6)

Table 3

Definitions of the relevant average particle sizes and volumes, based on their size distribution functions.

$\langle r\rangle = \int f_{\text{NP}}(r)r\,\mathrm{d}r$	$\langle r\rangle_{\text{act}} = \int_r \int_t f_{\text{NP}}(r)\Lambda(r,t)r\,\mathrm{d}t\,\mathrm{d}r$
$\langle V\rangle = \frac{4\pi}{3}\int f_{\text{NP}}(r)r^3\,\mathrm{d}r$	$\langle V\rangle_{\text{act}} = \frac{4\pi}{3}\int_r \int_t f_{\text{NP}}(r)\Lambda(r,t)r^3\,\mathrm{d}t\,\mathrm{d}r$
$\langle r^3\rangle^{1/3} = \sqrt[3]{\frac{3}{4\pi}\langle V\rangle}$	$\langle r^3\rangle_{\text{act}}^{1/3} = \sqrt[3]{\frac{3}{4\pi}\langle V\rangle_{\text{act}}}$

Within the Chantrell approximation, the upper boundary also moves towards larger radii as time progresses, in contrast to the MSM model. Within that approximation it follows from (32) and (31) that

$$B_{\text{MRX}}(t) \propto \Delta V \propto r_H^3 - r_0^3 \propto \ln\left(1 + \frac{\tau_c}{t}\right). \tag{33}$$

The MSM expression differs from the result obtained with sharp window boundaries in the sense that the constant τ_c in (33) is effectively time-dependent.

In Fig. 5 we show, on a logarithmic time scale, the evolution of the left and right boundaries (defined as their half-height points) of the window function for a realistic set of system parameters.

3.6. MRX decay of SPIONs with finite size distributions

For particle size distributions $f_{\text{NP}}(r)$ that are very broad compared to the width of the window function during the MRX recording time, the complete model and the sharp window approach are expected to yield similar, albeit not identical, decay curves $B_{\text{MRX}}(t)$, for which (33) gives a good description. This is evidenced by the left graph of Fig. 6. For narrower distributions in which one of the window function boundaries coincides with, or moves through the edge of the $f_{\text{NP}}(r)$ distribution, significant deviations of the two model predictions occur as evidenced by the middle and right graphs of Fig. 6.

4. MRX data analysis

We consider a SPION sample of density ρ and mass m_{tot} that was magnetised during a time T_M in an external field H_M. The magnetic induction $B_{\text{MRX}}(t)$ produced by the sample is detected by

a magnetometer placed at a distance R ($\hat{R} = \hat{H}_M$) from the sample. As shown in Section 3 the magnetic induction $B_{\text{MRX}}(t)$ measured by the sensor at time t (MRX signal) following the switching off of the magnetising field H_M is given by

$$B_{\text{MRX}}(t) =$$
$$\frac{\mu_0}{2\pi R^3}\frac{m_{\text{tot}}}{\rho}\frac{M_s}{\langle r^3\rangle}\int_0^\infty L(H_M, M_s; r)\Lambda(H_M, M_s, K, T_M; r, t)f_{\text{SZ}}(r)r^3\,\mathrm{d}r \tag{34}$$

with

$$\langle r^3\rangle = \int_0^\infty f_{\text{SZ}}(r)r^3\,\mathrm{d}r. \tag{35}$$

In contrast to Eq. (25), we have introduced explicitly in the function arguments the relevant experimental and system parameters, and have further replaced the general size distribution $f_{\text{NP}}(r)$ by the Schulz–Zimm distribution, $f_{\text{SZ}}(r)$, used for the characterisation of our samples (cf. Section 2).

The analysis of the experimental MRX data is based on Eq. (34). For computational purposes we replace the integrals in that expression by the finite sums

$$B_{\text{MRX}}(t) = aM_s\frac{\sum_i r_i^3 L(H_M, M_s; r_i)\Lambda\left(H_M, M_s, K, T_M; r_i, t\right)f_{\text{SZ}}(r_i)}{\sum_i r_i^3 f_{\text{SZ}}(r_i)}. \tag{36}$$

Rather than using the particle size distributions given by the experimental histograms of Fig. 1, we use the fitted Schulz–Zimm functions, discretised in steps $\Delta r = r_{i+1} - r_i$ of 0.1 nm in the interval from 1 to 30 nm. This step size is small compared to all relevant spatial scales, i.e., widths of $f_{\text{SZ}}(r)$ and sharpness of the window boundaries. Recalling that our magnetometers measure the field on an absolute scale and comparing Eqs. (34) and (36) one sees that the parameter a is proportional to the total mass m_{tot} of nanoparticles in the sample.

Our experimental data is a set of relaxation curves, each consisting of a time series $B_j = B(t_j)$, recorded for the six samples (A–F). We recorded MRX traces with four different iron contents (ranging from 1 to 8 mg) in every sample, so that the total data set consist of 24 MRX traces. In Eq. (36) the magnetising field and duration are known experimental parameters with values $\mu_0 H_M = 27$ mT and $T_M = 3$ s, while K, M_s, and a are the parameters of interest in this study that are determined by fitting Eq. (34) to the experimental data. In order to avoid confusion further down we denote the fit parameters and the fit function by a tilde $\sim$, viz.,

$$\widetilde{B}_{\text{MRX}}(t) = \widetilde{a}\widetilde{M}_s\frac{\sum_i r_i^3 L(H_M, \widetilde{M}_s; r_i)\Lambda(H_M, \widetilde{M}_s, \widetilde{K}, T_M; r_i, t)f_{\text{SZ}}(r_i)}{\sum_i r_i^3 f_{\text{SZ}}(r_i)} + \widetilde{b}, \tag{37}$$

where we have added a constant offset $\widetilde{b}$ that takes the laboratory background field into account.

Below we will describe the fits of our data with the MSM function (37), as well as with the logarithmic decay law of Chantrell
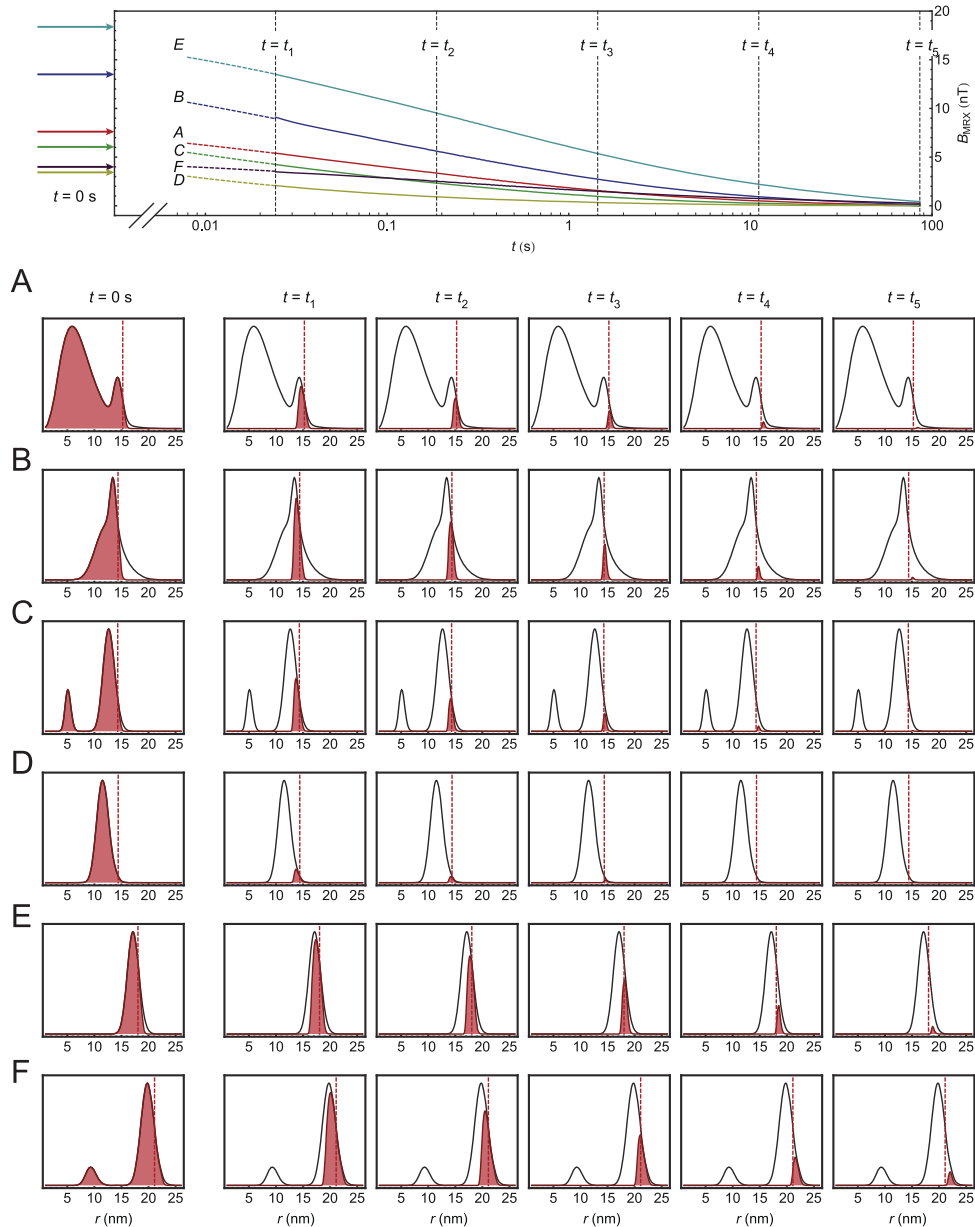
Fig. 8. Top: Modelled decays of the SPION samples' magnetic induction (traces for the highest concentration for each sample type). Bottom: Schulz–Zimm size distributions (solid lines) and distributions of active particles (shaded areas) that effectively contribute to the MRX signals at different times. The vertical dashed lines represent $\langle r \rangle_{\text{act}}$ (cf. Table 1).

$$\widetilde{B}_{\text{MRX}}^{(C)}(t) = \tilde{a}_C \ln\left(1 + \frac{\widetilde{\tau}_c}{t}\right) + \widetilde{b}_C, \tag{38}$$

introduced by Eq. (33).

5. Results

5.1. MRX decay

Fig. 7 shows the MRX signals from all the six samples in their highest iron concentration. Data are shown as dots together with 4-parameter ($\widetilde{K}$, $\widetilde{M}_s$, $\tilde{a}$, $\tilde{b}$) fits by the MSM function (37) (fit parameters collected in Table 1) and 3-parameter ($\widetilde{\tau}_c$, $\tilde{a}_C$, $\widetilde{b}_C$) fits by the logarithmic decay law (38), whose parameters are collected in Table 2. The lower parts of the individual graphs in Fig. 7 show the corresponding fit residuals. For a better assessment of the fit

quality at different time scales we have represented all data on lin–lin, log–lin, and log–log scales. One sees that the MSM function (37) gives a better description of the experimental data at small and large times than the logarithmic decay law (38).

In Tables 1–3 we also provide several parameters describing the particle size distributions, where the subscript 'act' refers to the magnetically active fraction of the particles that is selected by the window dynamic.

5.2. Window function dynamics – experiment

With the experimentally determined parameters $\widetilde{K}$ and $\widetilde{M}_s$ we can now visualise the window dynamics that underlies the MRX decay. The red shaded areas in the graphs of Fig. 8 represent the product $f_{\text{SZ}}(r)\Lambda(r, t)$ of the particle size distribution and the window function for five selected times t_i during the observed magnetisation decay. The top graph shows the MRX signals in the explored time interval (24 ms < t < 87 s) as well as the back-
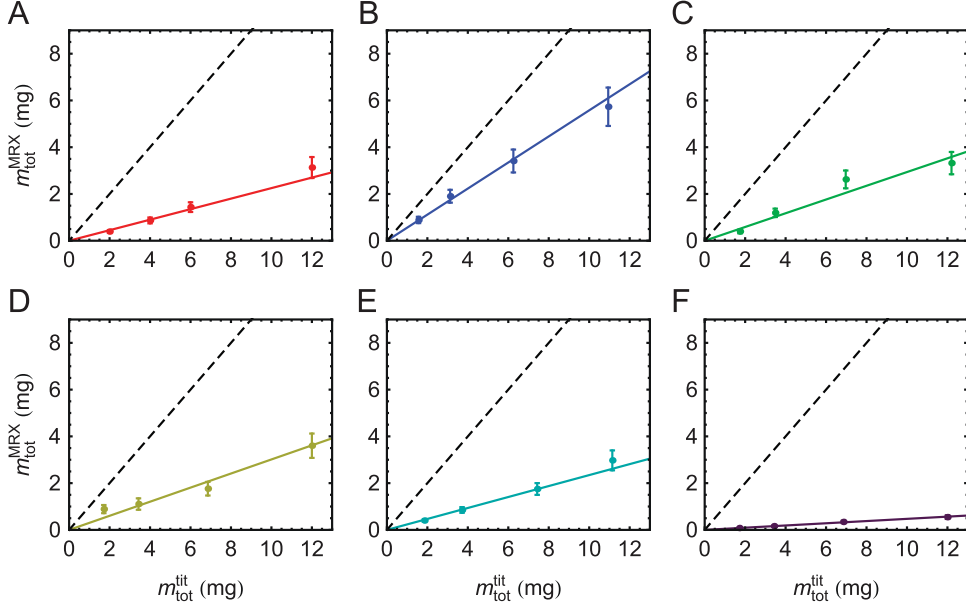
Fig. 9. Dependence of the magnetically active mass fraction inferred from fits to the MRX signals on the maghemite mass determined by titration. Data are shown for different dilutions together with linear fits. The dashed line represents $m_{tot}^{MRX} = m_{tot}^{tit}$.

Table 4
Dependence of the magnetically active mass fraction inferred from fits to the MRX signals on the maghemite mass determined by titration for evaluated samples.

Sample	$\langle V \rangle_{act}$ (10^3 nm^3)	$m_{tot}^{MRX}/m_{tot}^{tit}$
A	14.8	0.22
B	12.4	0.56
C	12.3	0.29
D	12.5	0.30
E	24.6	0.23
F	39.4	0.05

extrapolated fitted MRX functions and value $B_{MRX}(t = 0)$ (marked by horizontal arrows). The leftmost column of the lower graphs gives $f_{SZ}(r)\Lambda(r, 0)$, i.e., the magnetised fraction of particles at the end of the magnetisation process that is unobservable because of the detector dead time.

5.3. Magnetised mass fraction and total sample mass reconstrunction

From Eqs. (34) and (37) it follows that the fit parameter $\tilde{a}$ is proportional to total mass of the nanoparticles m_{tot}:

$$m_{tot}^{MRX} = \frac{3R^3}{2\mu_0}m_{NP}\tilde{a} = \frac{3R^3}{2\mu_0}\rho\langle V \rangle \tilde{a}. \tag{39}$$

In Fig. 9 we compare, for each sample, the total mass of the sample, m_{tot}^{MRX}, inferred from the fit parameter $\tilde{a}$, to the sample mass , $m_{tot}^{tit} = m_{Fe}^{tit}/\varepsilon$, where $\varepsilon = 0.7$ is the fractional iron content of an Fe_2O_3 molecule, and m_{Fe}^{tit} the iron mass in the sample determined by titration (cf. Section 2.1).

We first note that for all samples $m_{tot}^{MRX} \propto m_{tot}^{tit}$. However, none of the samples obeys the anticipated $m_{tot}^{MRX} = m_{tot}^{tit}$ dependence, although $m_{tot}^{MRX} < m_{tot}^{tit}$ confirms that the results are physically realistic (Table 4). This observation shows that the samples contain particles that either do not produce a magnetic field or whose magnetisation does not relax according to the MSM decay law. We cannot rule out, although it is unlikely, that the samples contain much larger particles that were not detected by the TEM characterisation process.

The graphs of Fig. 9 reveal an increasing deviation from the slope=1 dependence with increasing particle size. One may assume that the larger particles have a multidomain structure, whose ferromagnetic behaviour is not described by our model. However, we can rule out this hypothesis since maghemite is known [34] to exist in single domain forms up to radii $\langle r \rangle \sim 35$ nm, larger than the particles in our experiments.

Another, also less likely hypothesis, is the assumption that the samples contain a fraction of particles that obey a Brownian, rather than a Néel relaxation law. In fact, the shell of SPIONs obtained by thermal decomposition consists of oleic acid covalently bound to the particle surface together with unbound free oleic acid [35,36]. This encapsulating liquid layer may act as embedding agent and prevail after drying at low temperatures (60 °C) resulting in a paste-like component with a high, albeit finite viscosity, leading to fast relaxation that is unobservable with the dead-time of our detector.

In our opinion, the most likely explanation of our observations is the assumption that the larger samples contain a substantial amount of magnetite [26], which cannot be magnetised as easily as maghemite and thus cannot be observed in our experiments.

Despite of those discrepancies we may claim that our MRX measurement and analysis method allows us to infer the samples' iron content on an absolute scale within a factor of ≈ 5. We stress that the relative scaling of the total sample mass under dilution can be estimated with an accuracy of $\approx 10\%$.

### 5.4. Extracting the saturation magnetisation M_s and anisotropy constant K

The 4-parameter fits of the MRX data by the MSM function yield values for $\tilde{a}$, $\tilde{b}$, $\widetilde{M}_s$, and $\widetilde{K}$. In order to make sure that these global fits do not converge to local minima we have performed the following systematic study. We define a discrete grid of reasonable values $2 < K^{(j)} < 10$ kJ/m^3 and $0 < M_s^{(j)} < 60$ kA/m and fit, for each pair of fixed $K^{(j)}$ and $M_s^{(j)}$ values the function (37) to the data. In that case the two remaining fit parameters $\tilde{a}$ and $\tilde{b}$ can be inferred using a linear regression. We define the quantity $\chi^2 = \sum \delta B_{MRX}^2 \equiv \sum (B_{MRX}^{(exp)} - \widetilde{B}_{MRX})^2$, and use $1/\chi_N^2 \equiv \min(\chi^2)/\chi^2 \in [0, 1]$ as a measure for the fit quality.
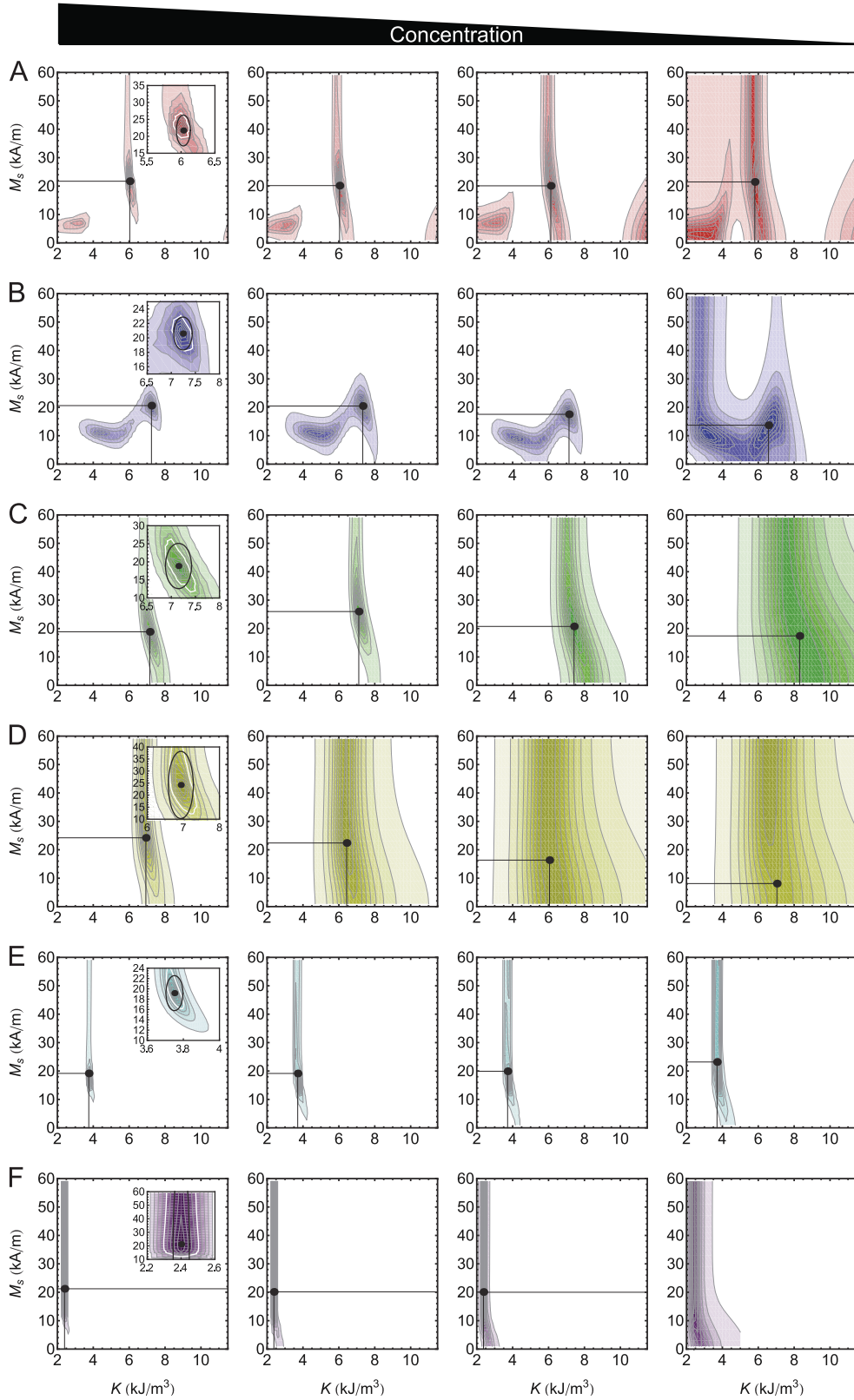
Fig. 10. Determination of K and M_s values from 2- and 4-parameter fits of 24 experimental data sets as described in the text. The contour lines represent $1/\chi_N^2$ values when the parameters $\tilde{a}$ and $\tilde{b}$ are fitted on a mesh of fixed K and M_s values. Insets: The solid white lines represent the $1/\chi_N^2 = 1/2$ confidence region boundaries. The black dots and black ellipses represent the best (K, M_s) values obtained by 4-parameter fits.

We have applied this two-parameter fit procedure to all 24 experimental MRX traces. Fig. 10 shows the corresponding contour plots of constant $1/\chi_N^2$ values. The inserts of Fig. 10 for the highest iron concentrations are zooms into the regions near the corresponding minimal χ^2 values. The black contour lines in the inserts represent the contours for which $1/\chi_N^2 = 1/2$, while the smooth
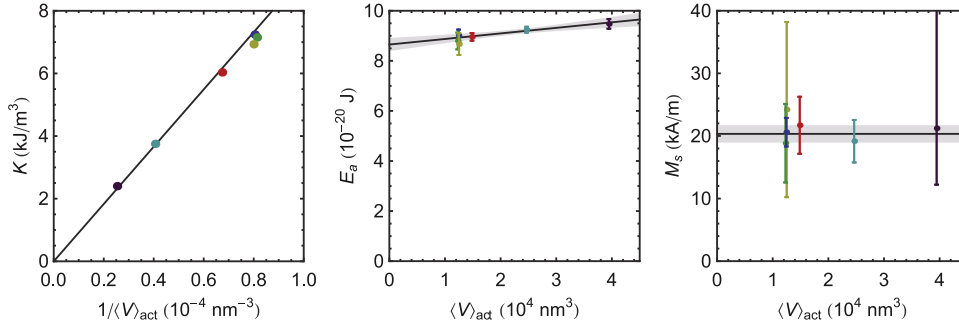
Fig. 11. Dependence of the fitted anisotropy constant K on the inverse of the average particle volume (left), anisotropic energy E_a (centre) and saturation magnetisation M_s (left) on the average particle volume.
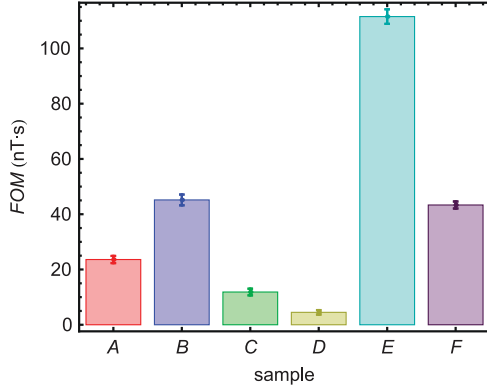
Fig. 12. Figure of merit (*FOM*) defined by (40) of all investigated samples. Uncertainties are defined by the error of the background level estimations in (37).

ellipses represent the errors of the four-parameter fits of the MRX data. The fact that the regions of confidence produced by the two fit approaches show a large overlap demonstrates the consistency of the methods.

For most of the samples the maximal $1/\chi_N^2$ values are located in a compact region of the $K-M_s$ space. While the relative errors on the anisotropy constant K are less than 5%, the corresponding relative uncertainties on M_s are significantly larger. This effect is particularly pronounced for sample D, for which no closed contour lines are found in the studied parameter range. As expected, the regions of confidence of all samples become wider as the iron content is lowered. Within the uncertainties defined by the $1/\chi_N^2 = 1/2$ boundary, the M_s and K values show no dependence on the particle concentration.

The values of K and M_s determined in this way are listed, together with their uncertainties, in Table 1. Fig. 11 shows that the anisotropy constant K, usually considered as a particle independent material parameter, is proportional to the inverse of the average volume of the magnetically active particles $\langle V \rangle_{\text{act}}$. As a consequence, the anisotropy energy $E_a = K \langle V \rangle_{\text{act}}$ of the active particles weakly depends on the particle volume (central graph of Fig. 11) and is equal to $8.65(10) \times 10^{-20}$ J as extrapolated to $\langle V \rangle_{\text{act}} = 0$, defined in Table 3.

In contrast to the latter observation the right graph of Fig. 11 shows that the saturation magnetisation M_s is volume independent, with an average value of $M_s = 20.3(1.2)$ kA/m.

5.5. Figure of merit

In order to compare the relative merits of the different samples in view of their use for MRX detection we introduce a figure of merit defined by

$$FOM = \int_{t_1 = 24 \text{ ms}}^{t_5 = 87 \text{ s}} B_{\text{MRX}}(t) \, dt, \tag{40}$$

where the integration limits t_1 and t_5 refer to the beginning and end of the magnetisation recordings in Fig. 7. We have calculated this figure of merit for all samples based on the experimental data, after subtraction of the fitted offset field value $\tilde{b}$ in Eq. (37). The results are represented in Fig. 12 and show that sample E is the best suited under the used experimental conditions. This result can be understood based on the fact that sample E has the largest magnetisation, and thus produces the largest induction B_{MRX} at time $t=0$. In addition, sample E features, together with sample F, the longest relaxation time τ_C (Table 2). The initial magnetisation of sample F is rather small because of the large particle size that is reflected by the very small active mass fraction of that sample (Fig. 9). Sample B has a slightly lower initial magnetisation than sample E, while having a significantly shorter relaxation time, a feature shared with samples A, C and D. In consequence these particles have a reduced *FOM*.

We have tried, without success, to record MRX signal from samples with $\langle r \rangle < 10$ nm and $\langle r \rangle > 25$ nm. Considering our experimental parameters $T_M = 3$ s, $\mu_0 H_M = 27$ mT, and $\tau_D = 25$ ms, the MSM shows indeed that the magnetic field $B_{\text{MRX}}(t = 0)$ is below the detection limit of our magnetometer.

6. Discussion

We have shown that atomic magnetometers can be used to record MRX data in the sub-nT range using a moderately shielded environment. The high quality of the signals has allowed us to infer material parameters of various SPION samples and to carry out a detailed study of the size dependence of their magnetorelaxation behaviour. As a result, we have determined the optimal size distribution under our experimental conditions in which the particles were magnetised in a field of 27 mT for 3 s.

We stress that the optimal SPIONs' size for a given MRX application depends very much on the magnetisation (H_M and T_M) and detection (τ_D) conditions, and that it makes no sense to speak about ideal particle size without specifying those experimental parameters.

The use of SPIONs for biomedical imaging based on MRX measurements requires not only that biochemical/biophysical properties fulfill the conditions of the targeted application but also puts constraints onto the material parameters, such as the saturation magnetisation M_S and anisotropy constant K. The magnetic field produced by the particles, i.e., their

magnetisation should decay on a time scale that is sufficiently long to overcome the limitations imposed by the unavoidable dead time of the magnetometer system. In principle, our magnetometer has a dead time of ≈ 1 ms. However, because of the aluminium shield, our gradiometer senses residual magnetic field gradients oscillating at 50 Hz at the level of ≈ 20 nT. These oscillations are suppressed numerically in data processing. As a result our system has an effective dead time of ≈ 24 ms.

Since the relaxation times grow with particle size (both in the Néel and Brown cases), the finite magnetometer dead time implies that only particles above a certain size effectively contribute to the MRX signal. In imaging applications one wishes to distinguish particles bound to biological entities whose MRX is determined by the Néel relaxation time τ_N from particles embedded in biological fluid assumed to show fast Brownian relaxation (τ_B). An efficient distinction of the particles' environment calls for $\tau_N \hat{a}^a \mathcal{C} \tau_B$, which therefore imposes a certain minimal SPION size $\langle r \rangle > 11$–12 nm. On the other hand, particles that are too large imply a longer relaxation time and hence require a stronger magnetising field and a longer magnetisation time. Our studies have shown that particles with $\langle r \rangle > 18.6$ nm (sample F) yield practically no signal, while a maximal signal and slowest relaxation was found for particles with $\langle r \rangle = 17.2$ nm. Our findings are well supported by model calculations based on the Néel–Brown–Chantrell approach, that describes the complex interplay of window function dynamics and particle size distributions.

As a surprising result we have found that the anisotropy constant K is inversely proportional to the magnetically active particle volume, implying an active volume independence of the anisotropy energy E_a. We note that size dependent K-values have been reported before (see, e.g., [26,37] and references therein), but that there is, to our knowledge, no satisfactory universal theoretical model explaining such a behaviour [34]. On the other hand we found that, within error

bars, the saturation magnetisation M_s is independent on particle size.

## Appendix A. Total energy of uniaxial SPIONs

In order to illustrate the relative importance of the anisotropy energy and the magnetic energy, we consider the simplest case of a uniaxial crystal for which the anisotropy energy is well approximated by [32]

$$E_a(\theta_c) = KV\sin^2\theta_c, \tag{A.1}$$

where K is the (first) anisotropy constant and θ_c the angle between $\vec{\mu}_p$ and the easy axis $\hat{c}$. When $\hat{c}$ is oriented along $\vec{H}$, the total energy becomes

$$E_{tot}(\theta) = KV\left(\sin^2\theta - 2h\cos\theta\right), \tag{A.2}$$

a dependence illustrated in Fig. A13. For $H = 0$ the total energy has two distinct (equivalent) minima that occur at $\theta = 0$ and π, respectively. For $H \neq 0$ one sees that the anisotropy field H_K represents the external field value, above which $E_{tot}(\theta)$ has only a single minimum, occurring at $\theta = 0$, i.e., when $\vec{H}$ is along the easy axis.
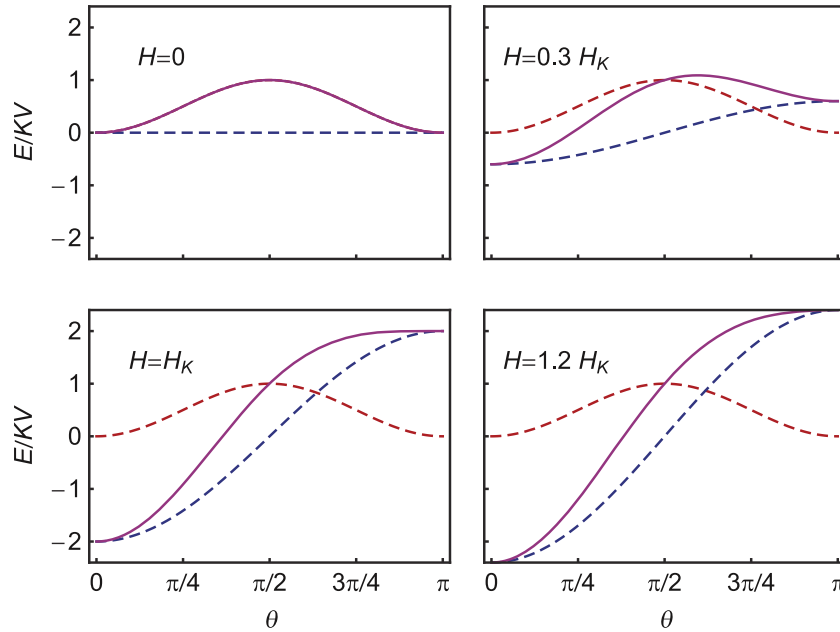
Fig. A13. Angular dependence of the total energy E_{tot} (solid magenta line) of a magnetic nanoparticle in an external magnetic field H. The dashed red and blue lines represent the anisotropy energy and magnetic energy, respectively. (For interpretation of the references to colour in this figure caption, the reader is referred to the web version of this paper.)

References

[1] T. Neuberger, B. Schopf, H. Hofmann, M. Hofmann, B. von Rechenberg, Superparamagnetic nanoparticles for biomedical applications: possibilities and limitations of a new drug delivery system, J. Magn. Magn. Mater. 293 (1, SI) (2005) 483–496. http://dx.doi.org/10.1016/j.jmmm.2005.01.064 5th International Conference on Scientific and Clinical Applications of Magnetic Carriers, Lyon, France, MAY 20–22, 2004.

[2] M. Arruebo, R. Fernndes-Pacheco, M.R. Ibarra, J. Santamaria, Magnetic nanoparticles for drug delivery, Nano Today 2 (3) (2007) 22–32.

[3] S.-H. Huang, R.-S. Juang, Biochemical and biomedical applications of multifunctional magnetic nanoparticles: a review, J. Nanopart. Res. 13 (10) (2011) 4411–4430. http://dx.doi.org/10.1007/s11051-011-0551-4.

[4] N. Lee, T. Hyeon, Designed synthesis of uniformly sized iron oxide nanoparticles for efficient magnetic resonance imaging contrast agents, Chem. Soc. Rev. 41 (7) (2012) 2575–2589. http://dx.doi.org/10.1039/c1cs15248c.

[5] A.E. Deatsch, B.A. Evans, Heating efficiency in magnetic nanoparticle hyperthermia, J. Magn. Magn. Mater. 354 (2014) 163–172. http://dx.doi.org/10.1016/j.jmmm.2013.11.006.

[6] M. Mahmoudi, S. Sant, B. Wang, S. Laurent, T. Sen, Superparamagnetic iron oxide nanoparticles (SPIONs): development, surface modification and applications in chemotherapy, Adv. Drug Deliv. Rev. 63 (1–2) (2011) 24–46. http://dx.doi.org/10.1016/j.addr.2010.05.006.

[7] B. Gleich, J. Weizenecker, Tomographic imaging using the nonlinear response of magnetic particles, Nature 435 (2005) 1214–1217.

[8] Bruker Corporation, Innovation from Bruker and Philips Brings Entirely New Technology to the Preclinical Imaging Market, 2013. URL: ⟨http://www.bruker.com/news-records/single-view/article/bruker-announces-the-worlds-first-preclinical-magnetic-particle-imaging-mpi-system.html⟩

[9] F. Wiekhorst, U. Steinhoff, D. Eberbeck, L. Trahms, Magnetorelaxometry assisting biomedical applications of magnetic nanoparticles, Pharm. Res. 29 (5) (2012) 1189–1202. http://dx.doi.org/10.1007/s11095-011-0630-3.

[10] L. Néel, Thorie du tranage magntique des ferromagntiques en grains fins avec applications aux terres cuites, Ann. Geophys. (C.N.R.S.) 5 (1949) 99–136. http://dx.doi.org/10.1103/PhysRev.130.1677.

[11] W. Brown, Thermal fluctuations of a single-domain particle, Phys. Rev. 130 (5) (1963) 1677–1686. http://dx.doi.org/10.1103/PhysRev.130.1677.

[12] R. Kotitz, W. Weitschies, L. Trahms, W. Brewer, W. Semmler, Determination of the binding reaction between avidin and biotin by relaxation measurements of magnetic nanoparticles, J. Magn. Magn. Mater. 194 (1–3) (1999) 62–68. http://dx.doi.org/10.1016/S0304-8853(98)00580-0 2nd International Conference on Scientific and Clinical Applications of Magnetic Carriers (SCAMC2), Cleveland, Ohio, MAY 28–30, 1998.

[13] E. Romanus, M. Huckel, C. Gross, S. Prass, W. Weitschies, R. Brauer, P. Weber, Magnetic nanoparticle relaxation measurement as a novel tool for in vivo diagnostics, J. Magn. Magn. Mater. 252 (1–3) (2002) 387–389. http://dx.doi.org/10.1016/S0304-8853(02)00645-5 9th International Conference on Magnetic Fluids, Bremen, Germany, July 23–27, 2001.

[14] D. Eberbeck, M. Kettering, C. Bergemann, P. Zirpel, I. Hilger, L. Trahms, Quantification of the aggregation of magnetic nanoparticles with different polymeric coatings in cell culture medium, J. Phys. D: Appl. Phys. 43 (40) (2010) 405002. http://dx.doi.org/10.1088/0022-3727/43/40/405002.

[15] N.L. Adolphi, D.L. Huber, H.C. Bryant, T.C. Monson, D.L. Fegan, J. Lim, J.E. Trujillo, T.E. Tessier, D.M. Lovato, K.S. Butler, P.P. Provencio, H.J. Hathaway, S.A. Majetich, R.S. Larson, E.R. Flynn, Characterization of single-core magnetite nanoparticles for magnetic imaging by SQUID relaxometry, Phys. Med. Biol. 55 (19) (2010) 5985–6003. http://dx.doi.org/10.1088/0031-9155/55/19/023.

[16] E. Flynn, H. Bryant, A biomagnetic system for in vivo cancer imaging, Phys. Med. Biol. 50 (6) (2005) 1273–1293. http://dx.doi.org/10.1088/0031-9155/50/6/016.

[17] N.L. Adolphi, D.L. Huber, J.E. Jaetao, H.C. Bryant, D.M. Lovato, D.L. Fegan, E.L. Venturini, T.C. Monson, T.E. Tessier, H.J. Hathaway, C. Bergemann, R.S. Larson, E.R. Flynn, Characterization of magnetite nanoparticles for SQUID-relaxometry and magnetic needle biopsy, J. Magn. Magn. Mater. 321 (10) (2009) 1459–1464. http://dx.doi.org/10.1016/j.jmmm.2009.02.067 7th International Conference on Scientific and Clinical Applications of Magnetic Carriers, Vancouver, Canada, MAY 20–24, 2008.

[18] H.J. Hathaway, K.S. Butler, N.L. Adolphi, D.M. Lovato, R. Belfon, D. Fegan, T.C. Monson, J.E. Trujillo, T.E. Tessier, H.C. Bryant, D.L. Huber, R.S. Larson, E.R. Flynn, Detection of breast cancer cells using targeted magnetic nanoparticles and ultra-sensitive magnetic field sensors, Breast Cancer Res. 13 (5) (2011) R108.

[19] M.V. Romalis, H.B. Dang, Atomic magnetometers for materials characterization, Mater. Today 14 (6) (2011) 258–262.

[20] G. Bison, N. Castagna, A. Hofer, P. Knowles, J.L. Schenker, M. Kasprzak, H. Saudan, A. Weis, A room temperature 19-channel magnetic field mapping device for cardiac signals, Appl. Phys. Lett. 95 (17) (2009) 173701. http://dx.doi.org/10.1063/1.3255041.

[21] T.H. Sander, J. Preusser, R. Mhaskar, J. Kitching, L. Trahms, S. Knappe, Magnetoencephalography with a chip-scale atomic magnetometer, Biomed. Opt. Express 3 (5) (2012) 981–990.

[22] S. Knappe, T.H. Sander, O. Kosch, F. Wiekhorst, J. Kitching, L. Trahms, Cross-validation of microfabricated atomic magnetometers with superconducting quantum interference devices for biomagnetic applications, Appl. Phys. Lett. 97 (13) (2010) 133703. http://dx.doi.org/10.1063/1.3491548.

[23] V. Lebedev, V. Dolgovskiy, B. Michen, A. Fink, G. Bison, A. Weis, Non-scanning magnetic field imaging with laser-pumped atomic magnetometer, Biomed. Eng. 58 (1) (2013) 663–664. http://dx.doi.org/10.1515/bmt-2013-4294, Tri-State Conference of the German-Swiss-and-Austrian-Society-for-Biomedical-Technology (BMT), Graz, AUSTRIA, 2013.

[24] C. Johnson, N.L. Adolphi, K.L. Butler, D.M. Lovato, R. Larson, P.D.D. Schwindt, E.R. Flynn, Magnetic relaxometry with an atomic magnetometer and SQUID sensors on targeted cancer cells, J. Magn. Magn. Mater. 324 (17) (2012) 2613–2619. http://dx.doi.org/10.1016/j.jmmm.2012.03.015.

[25] P. Liu, K. Skucha, M. Megens, B. Boser, A CMOS hall-effect sensor for the characterization and detection of magnetic nanoparticles for biomedical applications, IEEE Trans. Magn. 47 (10) (2011) 3449–3451. http://dx.doi.org/10.1109/TMAG.2011.2158600, Conference on International Magnetics (INTERMAG), Taipei, Taiwan, April 25–29, 2011.

[26] J. Park, K. An, Y. Hwang, J. Park, H. Noh, J. Kim, J. Park, N. Hwang, T. Hyeon, Ultra-large-scale syntheses of monodisperse nanocrystals, Nat. Mater. 3 (12) (2004) 891–895. http://dx.doi.org/10.1038/nmat1251.

[27] A.G. Roca, M.P. Morales, C.J. Serna, Synthesis of monodispersed magnetite particles from different organometallic precursors, IEEE Trans. Magn. 42 (10) (2006) 3025–3029. http://dx.doi.org/10.1109/TMAG.2006.880111 41st IEEE International Magnetics Conference (Intermag 2006), San Diego, CA, May 8–12, 2006.

[28] N. Castagna, G. Bison, G. Di Domenico, A. Hofer, P. Knowles, C. Macchione, H. Saudan, A. Weis, A large sample study of spin relaxation and magnetometric sensitivity of paraffin-coated Cs vapor cells, Appl. Phys. B: Lasers Opt. 96 (4) (2009) 763–772. http://dx.doi.org/10.1007/s00340-009-3464-5.

[29] S. Groeger, G. Bison, J. Schenker, R. Wynands, A. Weis, A high-sensitivity laser-pumped M-x magnetometer, Eur. Phys. J. D 38 (2) (2006) 239–247. http://dx.doi.org/10.1140/epjd/e2006-00037-y.

[30] R. Chantrell, S. Hoon, B. Tanner, Time-dependent magnetization in fine-particle ferromagnetic systems, J. Magn. Magn. Mater. 38 (2) (1983) 133–141. http://dx.doi.org/10.1016/0304-8853(83)90037-9.

[31] R. Chantrell, J. Popplewell, S. Charles, Measurements of particle-size distribution parameters in ferrofluids, IEEE Trans. Magn. 14 (5) (1978) 975–977. http://dx.doi.org/10.1109/TMAG.1978.1059918.

[32] L.D. Landau, L.P. Pitaevskii, E.M. Lifshitz, Electrodynamics of Continuous Media, Pergamon Press, Oxford, 1984.

[33] W.T. Coffey, Y.P. Kalmykov, Thermal fluctuations of magnetic nanoparticles: fifty years after Brown, J. Appl. Phys. 112 (12) (2012) 121301. http://dx.doi.org/10.1063/1.4754272.

[34] A.G. Kolhatkar, A.C. Jamison, D. Litvinov, R.C. Willson, T.R. Lee, Tuning the magnetic properties of nanoparticles, Int. J. Mol. Sci. 14 (8) (2013) 15977–16009. http://dx.doi.org/10.3390/ijms140815977.

[35] A. Willis, N. Turro, S. O'Brien, Spectroscopic characterization of the surface of iron oxide nanocrystals, Chem. Mater. 17 (24) (2005) 5970–5975. http://dx.doi.org/10.1021/cm051370v.

[36] Z.P. Chen, Y. Zhang, S. Zhang, J.G. Xia, J.W. Liu, K. Xu, N. Gu, Preparation and characterization of water-soluble monodisperse magnetic iron oxide nanoparticles via surface double-exchange with DMSA, Colloids Surf. A 316 (1–3) (2008) 210–216. http://dx.doi.org/10.1016/j.colsurfa.2007.09.017.

[37] F. Bodker, S. Morup, Size dependence of the properties of hematite nanoparticles, Europhys. Lett. 52 (2) (2000) 217–223. http://dx.doi.org/10.1209/epl/i2000-00426-2.